



# Ti(Ni,Cu) pseudobinary compounds as efficient negative electrodes for Ni–MH batteries



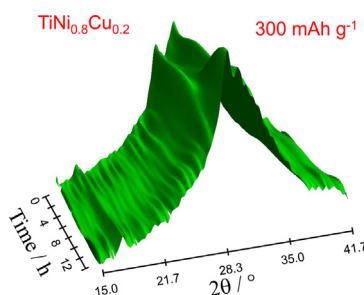
Hoda Emami<sup>1</sup>, Fermin Cuevas\*, Michel Latroche

CMTR/ICMPE/CNRS – UPEC, UMR 7182, 2-8 rue Henri Dunant, 94320 Thiais Cedex, France

## HIGHLIGHTS

- Hydrogenation properties of pseudobinary Ti(Ni,Cu) compounds are deeply investigated.
- Cu-substitution destabilizes the hydride phase and opens a wide miscibility gap.
- $\text{TiNi}_{0.8}\text{Cu}_{0.2}$  exhibits a high discharge capacity of  $300 \text{ mAh g}^{-1}$  with good cycle life.
- Electrochemical discharge capacities are two-fold higher than for binary TiNi.
- Ti(Ni,Cu) compounds are promising rare-earth free anodes for Ni–MH batteries.

## GRAPHICAL ABSTRACT



## ARTICLE INFO

### Article history:

Received 28 January 2014

Received in revised form

20 March 2014

Accepted 18 April 2014

Available online 2 May 2014

### Keywords:

Metal hydrides

Intermetallics

TiNi

Ni–MH batteries

In-situ neutron diffraction

## ABSTRACT

The effect of Ni by Cu substitution on the structural, solid–gas and electrochemical hydrogenation properties of TiNi has been investigated. Pseudo-binary  $\text{TiNi}_{1-x}\text{Cu}_x$  ( $x \leq 0.5$ ) compounds have been synthesized by induction melting. They crystallize in B2 structure above 350 K and either in B19' ( $x < 0.1$ ) or B19 ( $0.2 \leq x \leq 0.5$ ) at room temperature (RT). For all compounds, Pressure–Composition Isotherms at 423 K exhibit a single slopping plateau pressure within the range  $10^{-3}$ –1 MPa of hydrogen pressure revealing a metal to hydride transformation. Both the hydrogenation capacity and the hydride stability decrease with Cu-content. The hydrided pseudobinary compounds crystallize in the tetragonal S.G.  $I4/mmm$  structure as for TiNi hydride. The electrochemical discharge capacity increases with Cu content from  $150 \text{ mAh g}^{-1}$  for TiNi up to  $300 \text{ mAh g}^{-1}$  for  $\text{TiNi}_{0.8}\text{Cu}_{0.2}$  and then decreases again for larger Cu amounts. Electrochemical isotherms and *in-situ* neutron diffraction measurements at RT demonstrate that such a capacity increase results from a metal to hydride phase transformation in which the hydride phase is destabilized by Cu substitution. The  $\text{TiNi}_{0.8}\text{Cu}_{0.2}$  compound exhibits interesting cycling stability for 30 cycles and good high-rate capability at D/2 rate. This compound has promising electrochemical properties as compared to commercial  $\text{LaNi}_5$ -type alloys with the advantage of being rare-earth metal free.

© 2014 Elsevier B.V. All rights reserved.

\* Corresponding author. Tel.: +33 1 49 78 12 25; fax: +33 1 49 78 12 03.

E-mail addresses: [cuevas@icmpe.cnrs.fr](mailto:cuevas@icmpe.cnrs.fr), [fermin.cuevas@icmpe.cnrs.fr](mailto:fermin.cuevas@icmpe.cnrs.fr) (F. Cuevas).

<sup>1</sup> Current address: I2CNER, Kyushu University, Nishi-ku, Fukuoka 819-0395, Japan.

## 1. Introduction

In the later decades, metal hydrides have deserved extensive research since they can store higher amount of hydrogen per unit volume under moderate conditions of pressure and temperature

than high pressure tanks and liquid hydrogen [1,2]. Beside hydrogen storage applications, their use as active materials for the negative electrode of Ni–MH batteries is pursued [3–5]. Ni–MH batteries are a good alternative to Ni–Cd ones since the use of toxic cadmium is avoided and higher energy density (30–50%) is reached. Several metal-hydride forming compounds can be used in Ni–MH batteries such as  $\text{LaNi}_5$  ( $\text{AB}_5$ ),  $\text{La}_{5-x}\text{Mg}_x\text{Ni}_{19}$  ( $\text{A}_5\text{B}_{19}$ ),  $\text{La}_{2-x}\text{Mg}_x\text{Ni}_7$  ( $\text{A}_2\text{B}_7$ ),  $\text{La}_{1-x}\text{Mg}_x\text{Ni}_3$  ( $\text{AB}_3$ ),  $\text{ZrNi}_2$  ( $\text{AB}_2$ ) and  $\text{TiNi}$  ( $\text{AB}$ ), where A and B stand for metals forming stable and unstable hydrides, respectively [6]. Compounds of compositions ranging from  $\text{AB}_5$  to  $\text{AB}_3$ -type with typical discharge capacities of 320–380 mAh  $\text{g}^{-1}$  are today used as active materials in commercial Ni–MH batteries [7–9]. However, they all contain expensive rare-earth elements and their mass capacity is limited by their high molecular weight. TiNi-based compounds are lighter and do not contain strategic rare-earth elements and therefore are promising compounds for next generation of Ni–MH batteries.

TiNi is however most known for its outstanding shape memory properties which are based on a reversible martensitic transformation. This transition is a diffusionless structural transformation between a high temperature phase with cubic structure (CsCl-type, B2 in *structurebericht* designation) and a low temperature phase with monoclinic structure (B19'). As a shape memory alloy, TiNi has lots of mechanical and biomedical applications: piping, actuators, stents... [10–12]. Much less attention has been paid to the fact that TiNi can absorb significant amount of hydrogen (1.4 hydrogen atoms per formula unit H f.u. $^{-1}$ ) at normal conditions of temperature and pressure [13]. Furthermore, TiNi exhibits electrochemical activity and good resistance to corrosion in alkaline media [14]. For all these reasons, the use of TiNi as active material in Ni–MH batteries can be envisaged.

Unfortunately, the discharge capacity of binary TiNi is rather low. Gutjahr et al. reported that 230 mAh  $\text{g}^{-1}$  can be obtained at slow kinetic regime while using two-phase TiNi–Ti<sub>2</sub>Ni electrodes [15]. Interestingly, TiNi shows a good cycle life for more than 100 cycles. Chemical substitution in Ti or Ni sublattices can be effective to increase the discharge capacity. Thus, previous research in our group demonstrated that the hydrogenation capacity increases to 2.6 H f.u. $^{-1}$  for (Ti,Zr)Ni pseudobinary compounds leading to discharge capacities as high as 370 mAh  $\text{g}^{-1}$  at C/10 rate [16,17]. Unfortunately, the cycle-life of (Ti,Zr)Ni compounds is quite poor for the battery application.

In this study, the structural properties of Ti(Ni,Cu) intermetallic compounds (IMCs) as well as their solid–gas and electrochemical hydrogenation properties are investigated. We show that Cu substitution enhances the discharge capacity of binary TiNi up to 300 mAh  $\text{g}^{-1}$  at fast kinetic regime. Such a high capacity increase results from the destabilization of the hydride phase by the Cu substitution. These results demonstrate that the Ti(Ni,Cu) compounds, which do not contain costly rare-earth metals, are relevant materials for their use in commercial Ni–MH batteries.

## 2. Experimental methods

Cu substituted IMCs with nominal composition of  $\text{Ti}_{1.01}\text{Ni}_{0.99-x}\text{Cu}_x$  ( $x = 0, 0.1, 0.2, 0.3, 0.4$  and  $0.5$ ) were synthesized by induction melting in the form of alloy ingots. To ensure chemical homogeneity, the ingots were annealed at 1173 K for 4 weeks. Their chemical composition and microstructure were investigated by Electron Probe Micro Analysis (EPMA) with a Cameca SX-100 device. The martensitic transformation temperatures were determined by Differential Scanning Calorimetry (DSC) using a TA Q100 calorimeter in the range 200–400 K at the heating/cooling rate of 10 K  $\text{min}^{-1}$ . Samples were sealed in aluminum pans for this purpose. The crystal structure of IMCs and their hydrides was

characterized by powder X-ray diffraction (PXRD) with a  $\theta$ – $\theta$  Bragg–Brentano diffractometer (D8 Bruker) using  $\text{CuK}_\alpha$  radiation. For IMCs, diffraction data were obtained at RT and 473 K in powder samples. To produce the metallic powder, the samples were first embrittled by hydrogenation, next manually crushed to powder and then thermally desorbed by heating at 873 K under secondary vacuum. For hydrides, PXRD patterns were collected at RT.

Hydrogenation thermodynamics were characterized by Pressure Composition Isotherms (PCI) by the Sievert's method using home-made manometric benches. To speed up hydrogen absorption, the alloy ingots were first cut in to small pieces of  $\sim 1$  mm in thickness by using a low speed diamond saw, etched with HF 10% solution for 30 s and rinsed with ethanol. Samples were activated for three absorption/desorption cycles before PCI acquisition. Absorption was carried out at  $p_{\text{H}_2} = 5$  MPa,  $T = 423$  K and desorption at  $T = 773$  K under primary vacuum.

Electrochemical properties were determined by galvanostatic cycling at RT in one-compartment cell. Negative working electrodes (typical mass 300 mg) were made of Ti(Ni,Cu) powders sieved under 63  $\mu\text{m}$  and mixed with conductive black carbon and polytetrafluoroethylene (PTFE) in 90:5:5 weight ratio. This mixture was spread out in sheets of 0.25 mm thick and compressed onto a Ni current collector. A positive  $\text{NiOOH}/\text{Ni}(\text{OH})_2$  electrode was used as the counter electrode and the potential was measured versus a Hg/HgO reference electrode (Hg/HgO vs. SHE = 0.098 V). A poly-amide sheet was placed between the positive and negative electrode as a separator to avoid the electrical shortcuts. 6 M KOH aqueous solution was used as electrolyte both in the electrochemical cell and in the reference electrode to avoid  $\text{OH}^-$  concentration gradients. The galvanostatic cycling was performed at the rate of C/10 (full capacity C in 10 h) with a cutoff potential of  $-0.7$  V vs. Hg/HgO. Electrochemical isotherms were obtained at RT by the Galvanostatic Intermittent Titration Technique (GITT). For selected electrodes, high-rate capability studies were also carried out by galvanostatic charging at C/20 regime and subsequent discharge from 5D to D/20 rate.

To better understand the effect of Cu substitution on the electrochemical properties of TiNi, structural transformations of TiNi and  $\text{TiNi}_{0.8}\text{Cu}_{0.2}$  compounds were characterized during electrochemical deuteration by *in-situ* Neutron Powder Diffraction (NPD). The composite electrodes were made from  $\sim 3.5$  g of intermetallic powder using the same procedure as described before. The electrode sheets, about 1.5 mm in thickness, were rolled up on themselves to form cylinder of about 50 mm height and 10 mm diameter. The working electrode was placed between inner and outer cylindrical counter-electrode made of nickel, with silica sheaths as separators on each side of the working electrode. The working electrode was introduced in a specially designed silica cell [18] filled with electrolyte solution (5.5 M NaOD/D<sub>2</sub>O) and equipped with  $\text{Cd}/\text{Cd}(\text{OD})_2$  reference electrode ( $\text{Cd}(\text{OH})_2/\text{Cd}$  vs. SHE =  $-0.809$  V). The electrodes were charged at C/10 and discharged at D/10 rate with a cutoff potential of 0.5 V vs.  $\text{Cd}(\text{OH})_2/\text{Cd}$  otherwise specified. NPD data have been recorded at RT and ambient pressure with the High Resolution Powder Diffractometer for Thermal Neutrons (HRPT) in high sensitive mode at SINQ-PSI in Switzerland. The patterns were recorded by batch of 8 varying the detector angle by step of 0.15. Typical time acquisition was 225 s per pattern. The eight patterns were finally combined in one signal file leading to a time resolution of about 1800 s for each diffraction measurement. The diffraction patterns were sequentially refined by using the Rietveld method using the Fullprof software [19].

All electrochemical experiments were computer monitored using a VMP3 galvanostat from Biologic. Before running the experiments, electrochemical cells were pumped under primary vacuum in order to impregnate the working electrode with the electrolyte and to remove any gaseous molecules trapped in the electrode.

**Table 1**

Nominal and EPMA chemical composition of  $\text{Ti}_{1.01}\text{Ni}_{0.99-x}\text{Cu}_x$  alloy ingots. Standard deviations referred to the last digit are given in parenthesis.

$x$	Nominal composition	Main phase (EPMA)	Secondary phase (EPMA)
0	$\text{Ti}_{1.01}\text{Ni}_{0.99}$	$\text{Ti}_{1.01(1)}\text{Ni}_{0.95(7)}$	$\text{Ti}_{1.80(1)}\text{Ni}_{1.19(2)}$
0.1	$\text{Ti}_{1.01}\text{Ni}_{0.89}\text{Cu}_{0.1}$	$\text{Ti}_{1.02(1)}\text{Ni}_{0.88(1)}\text{Cu}_{0.10(2)}$	$\text{Ti}_{1.75(1)}\text{Ni}_{1.15(1)}\text{Cu}_{0.09(3)}$
0.2	$\text{Ti}_{1.01}\text{Ni}_{0.79}\text{Cu}_{0.2}$	$\text{Ti}_{1.02(1)}\text{Ni}_{0.78(2)}\text{Cu}_{0.19(1)}$	$\text{Ti}_{1.89(5)}\text{Ni}_{0.97(1)}\text{Cu}_{0.13(3)}$
0.3	$\text{Ti}_{1.01}\text{Ni}_{0.69}\text{Cu}_{0.3}$	$\text{Ti}_{1.02(1)}\text{Ni}_{0.68(4)}\text{Cu}_{0.30(1)}$	$\text{Ti}_{1.74(7)}\text{Ni}_{0.95(5)}\text{Cu}_{0.28(7)}$
0.4	$\text{Ti}_{1.01}\text{Ni}_{0.59}\text{Cu}_{0.4}$	$\text{Ti}_{1.02(1)}\text{Ni}_{0.58(4)}\text{Cu}_{0.39(3)}$	$\text{Ti}_{1.59(6)}\text{Ni}_{0.86(2)}\text{Cu}_{0.55(4)}$
0.5	$\text{Ti}_{1.01}\text{Ni}_{0.49}\text{Cu}_{0.5}$	$\text{Ti}_{1.02(1)}\text{Ni}_{0.48(7)}\text{Cu}_{0.49(1)}$	$\text{Ti}_{1.90(4)}\text{Ni}_{0.62(1)}\text{Cu}_{0.47(4)}$

### 3. Results and discussion

#### 3.1. Alloy characterization

##### 3.1.1. Chemical composition and microstructure

Phase occurrence and composition of alloy ingots are displayed in Table 1. All ingots contain AB-type Ti(Ni,Cu) as the main phase (typical content above 95%) and secondary  $\text{Ti}_2(\text{Ni,Cu})$   $A_2B$ -type precipitates. The composition of the main phase is close to the nominal one. Minor precipitation of  $A_2B$ -type phases in Ti-rich Ti(Ni,Cu) alloys is in agreement with the ternary Ti–Ni–Cu phase diagram [20]. The measured Ti-content of  $A_2B$ -type precipitates is much lower than expected ( $A/B$  ratio = 2) since their size is comparable with the spatial resolution of EPMA ( $\sim 1 \mu\text{m}$ ) as can be seen in back-scattered electron images (Fig S1 in Supplementary material).

##### 3.1.2. Thermal phase stability

The thermal phase stability of  $\text{TiNi}_{1-x}\text{Cu}_x$  IMCs has been analyzed by DSC at the second heating/cooling cycle and results are shown in Fig. 1. The martensitic transformation temperature and pathway depend on the Cu content. For binary TiNi ( $x = 0$ ), a single peak appears on cooling and heating due to the reversible  $B2 \rightarrow B19'$  structural transformation. In contrast, for  $x = 0.2$  two peaks both on cooling and heating appear. The high temperature peak is assigned to the  $B2 \rightarrow B19$  transformation while the lower peak corresponds to the  $B19 \rightarrow B19'$  transformation. The high temperature peak is larger and sharper than the low temperature peak. For the highest Cu content ( $x = 0.5$ ) only one peak appears which is assigned to the reversible  $B2 \rightarrow B19$  martensitic transformation. The thermal hysteresis is larger for  $B2 \rightarrow B19'$  than for the  $B2 \rightarrow B19$  martensitic transformation. From these results, the thermal phase stability map of  $\text{TiNi}_{1-x}\text{Cu}_x$  IMCs as a function of Cu

content is displayed in Fig. 1b. Transformation temperatures are compared to previous results reported by Nam et al. for  $\text{Ti}_{1.00}\text{Ni}_{1.00-x}\text{Cu}_x$  compounds [21]. In both studies the martensitic transformation temperatures decrease sharply for the  $B2 \rightarrow B19'$  transformation whereas those of  $B2 \rightarrow B19$  transition remain stable. However, the martensitic transformation temperatures in our work are about 30 K higher as compared to those of Nam et al. This difference is attributed to the use of Ti-rich composition in our study which currently leads to higher transformation temperatures [22].

#### 3.1.3. Crystal structure

The crystal structure of  $\text{Ti}_{1.01}\text{Ni}_{0.99-x}\text{Cu}_x$  alloys was first determined at 473 K by PXRD. The corresponding diffraction patterns are displayed in Fig. 2. At this temperature, the main phase is  $B2$  which yields a simple pattern with few diffraction peaks. This facilitates indexing of secondary phases: Ni-rich  $\text{Ti}_2(\text{Ni,Cu})$  phase with space group (S.G.)  $Fd-3m$  for low Cu contents ( $x \leq 0.3$ ) and Cu-rich  $\text{Ti}_2(\text{Cu,Ni})$  phase with S.G.  $I4/mmm$  for high Cu contents ( $x \geq 0.4$ ). The dependence of the unit-cell volume of the main  $B2$  phase with Cu content is given in the inset of Fig. 2. The cell parameter increases linearly with Cu content, a fact that concurs with the larger atomic radius of Cu as compared to Ni ( $r_{\text{Ni}} = 1.24 \text{ \AA}$ ,  $r_{\text{Cu}} = 1.28 \text{ \AA}$ ). This result anticipates the formation of pseudo-binary Ti(Ni,Cu) compounds with random and partial substitution of Ni by Cu atoms as will be later demonstrated by Rietveld analysis of the hydrided samples.

Fig. 3 shows the PXRD patterns of  $\text{Ti}_{1.01}\text{Ni}_{0.99-x}\text{Cu}_x$  alloys at RT. At low Cu contents ( $x \leq 0.1$ ) the main Ti(Ni,Cu) phase crystallizes in two polymorphs: the monoclinic  $B19'$  structure with  $P2_1m$  space group as major contribution, and residual  $B2$  phase in minor amount. In contrast, at high Cu contents ( $x \geq 0.2$ ), the Ti(Ni,Cu) phase crystallizes totally in the orthorhombic  $B19$  structure with S.G.  $Pmmn$ . The stabilization of the  $B19$  phase at high Cu-contents concurs with the DSC data shown in Fig. 1. The PXRD patterns were analyzed by the Rietveld method. Phase identification, abundance and cell parameters are displayed in Table S1 of Supplementary material. At  $x \leq 0.1$ , the martensitic phase  $B19'$  coexists with almost 13 wt.% of the parent  $B2$  cubic structure. However, at  $x \geq 0.2$  only the  $B19$  martensitic phase is detected. The dependence of the cell parameters and cell volume of the orthorhombic  $B19$  structure with Cu content is displayed in Fig. 3b. The cell parameters exhibit an anisotropic behavior:  $a$  and  $b$  cell parameters increase whereas the  $c$  lattice parameter decreases with

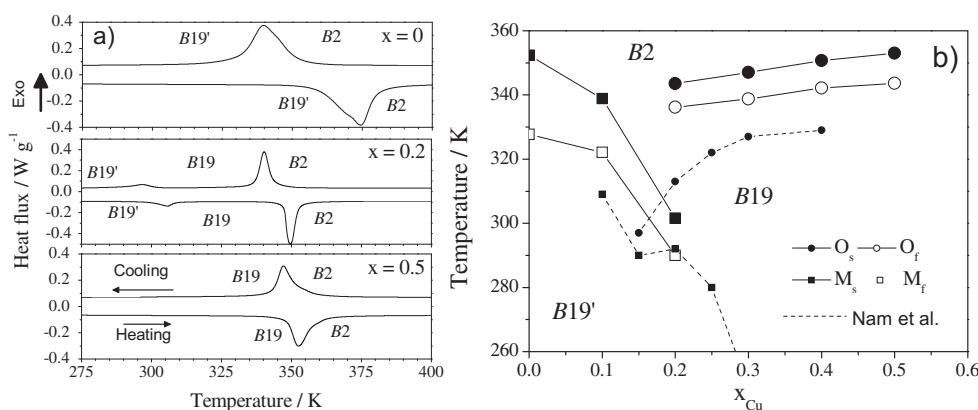


**Fig. 1.** a) DSC curves for  $\text{Ti}_{1.01}\text{Ni}_{0.99-x}\text{Cu}_x$  ( $x = 0, 0.2, 0.5$ ) samples in the second DSC run at a heating/cooling rate of  $10 \text{ K min}^{-1}$ . b) Martensitic transformation temperatures of  $\text{Ti}_{1.01}\text{Ni}_{0.99-x}\text{Cu}_x$  alloy ingots. Dashed line: results from Nam et al. [21]. O stands for  $B2 \rightarrow B19$  transformation and M stands for  $B2 \rightarrow B19'$  and  $B19 \rightarrow B19'$  phase transitions. Start and finish temperatures are denoted by s and f, respectively.

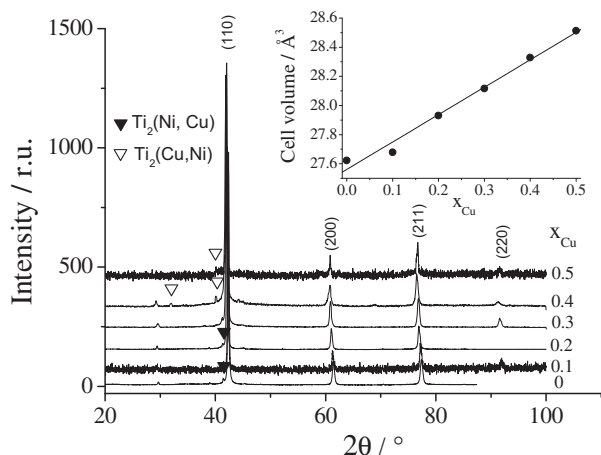


**Fig. 2.** PXRD diffraction patterns of  $\text{Ti}_{1.01}\text{Ni}_{0.99-x}\text{Cu}_x$  alloys at 473 K. Main diffraction peaks are indexed in the B2 structure. Peaks for secondary  $\text{Ti}_2(\text{Ni,Cu})$  and  $\text{Ti}_2(\text{Cu,Ni})$  phases are expressly marked. Inset: dependence of B2 unit cell volume versus the Cu content.

Cu content. The unit cell volume increases linearly with Cu content as already observed for the B2 phase (Fig. 2).

### 3.2. Solid–gas hydrogenation properties

#### 3.2.1. PCI curves and kinetics considerations

Fig. 4 displays the PCI absorption isotherms of  $\text{Ti}_{1.01}\text{Ni}_{0.99-x}\text{Cu}_x$  alloys at 423 K in the pressure range  $10^{-4}$ –1 MPa. A sloping plateau pressure starting at a hydrogen content of  $C_H = 0.35 \text{ H f.u.}^{-1}$  is observed. It is attributed to  $\alpha$ -metal to  $\beta$ -hydride phase transformation. The pressure of the plateau increases with Cu content showing that the hydride phase destabilizes with Cu substitution. This fact opposes to widely accepted geometrical models that state that hydride stability increases with enlarging of the intermetallic cell volume [23,24]. This implies that electronic rather than geometric factors govern the hydride stability of  $\text{Ti}(\text{Ni,Cu})$  IMCs. Indeed, we have recently demonstrated an analogous effect in Pd-substituted  $\text{TiNi}_{1-x}\text{Pd}_x$  alloys through DFT electronic calculations [25,26]. This concordance suggests, as a general rule, that electronic properties dictate the hydride stability of  $\text{TiNi}$ -based compounds.

It is worth mentioning that hydrogenation kinetics was found to be sluggish for hydrogen concentrations comprised within the

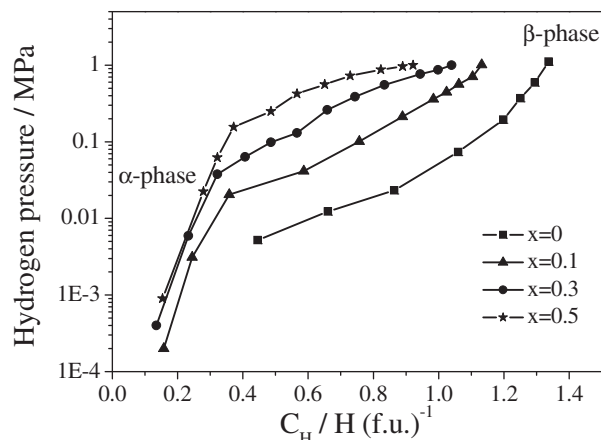


**Fig. 4.** PCI absorption curves of  $\text{Ti}_{1.01}\text{Ni}_{0.99-x}\text{Cu}_x$  ( $x = 0, 0.1, 0.3$  and  $0.5$ ) alloys at 423 K.

plateau pressure. Typically, PCI equilibrium pressures were obtained after resting time of 5 days at each sorption step. Interestingly, slow kinetics has also been reported by Kadel and Weiss for fully substituted  $\text{TiCu}$  [27]. It was attributed to decomposition of  $\text{TiCu}$  into  $\text{TiH}_2$  and  $\text{Cu}$  upon hydrogen absorption at high temperature (773–973 K). As will be later discussed,  $\text{Ti}(\text{Ni,Cu})$  intermetallics do not decompose upon hydrogenation at the temperatures used in this work but loss of crystallinity is detected, which may explain the observed kinetic behavior. Such crystallinity loss can decrease hydrogen diffusivity. In this respect, Mazzolai showed that by increasing the Cu content from 0.2 to 0.4 in  $\text{TiNi}_{1-x}\text{Cu}_x$  compounds, the hydrogen diffusion coefficient decreases from  $3 \times 10^{-7} \text{ m}^2 \text{ s}^{-1}$  to  $5 \times 10^{-8} \text{ m}^2 \text{ s}^{-1}$  [28].

#### 3.2.2. Hydrogen capacity and hydride crystal structure

The hydrogen capacity  $C_H$  of  $\text{Ti}_{1.01}\text{Ni}_{0.99-x}\text{Cu}_x$  alloys was determined at 423 K and 3.6 MPa of hydrogen pressure. Results are shown in Table 2 together with the crystal data of the formed hydrides.  $C_H$  decreases gradually from 1.40 ( $x = 0$ ) to 1.08 ( $x = 0.5$ )  $\text{H f.u.}^{-1}$  by increasing the Cu content. This decrease takes place in spite of the enlargement of the IMC cell volume with Cu content pointing out again that electronic rather than geometric factors dictate the thermodynamic hydrogenation properties of this system.

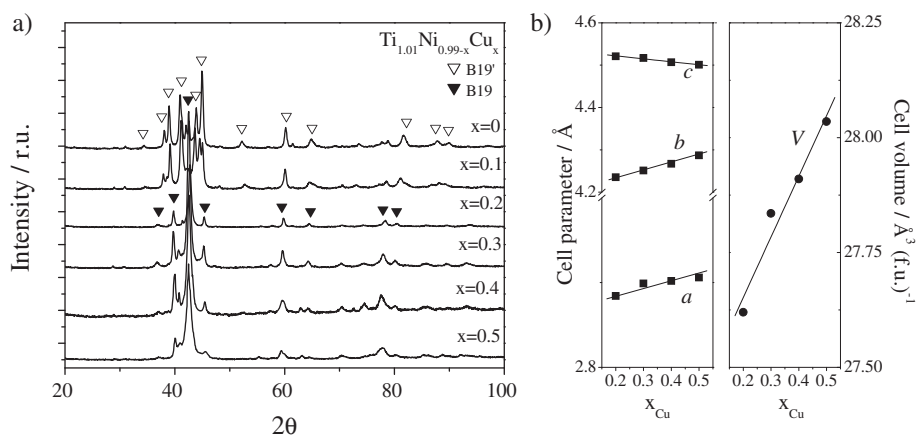


**Fig. 3.** a) Diffraction patterns of  $\text{Ti}_{1.01}\text{Ni}_{0.99-x}\text{Cu}_x$  alloys at RT. Diffraction peaks for the martensitic B19 and B19' phases are expressly labeled for  $x = 0$  and  $0.2$ . b) Evolution of cell parameters and cell volume of the B19 orthorhombic phase as a function of Cu content.

**Table 2**  
Hydrogen content ( $C_H$ ), cell parameters ( $a$ ,  $c$ ), cell volume ( $V$ ), hydrogen volume ( $V_H$ ) and Rietveld agreement factors ( $R_b$  and  $\chi^2$ ) of fully hydrogenated  $Ti_{1.01}Ni_{0.99-x}Cu_x$  samples. The standard deviations referred to the last digit are given in parenthesis.

$x$	Composition	$C_H$ ( $\text{\AA}^3 \text{ f.u.}^{-1}$ )	$a$ ( $\text{\AA}$ )	$c$ ( $\text{\AA}$ )	$2a/c$	$V$ ( $\text{\AA}^3 \text{ f.u.}^{-1}$ )	$V_H$ ( $\text{\AA}^3 \text{ H}^{-1}$ )	$R_b$ (%)	$\chi^2$
0	$Ti_{1.01}Ni_{0.99}H_{1.4}$	1.4	6.2255(6)	12.364(2)	1.007	29.95(1)	1.84	9.8	1.9
0.1	$Ti_{1.01}Ni_{0.89}Cu_{0.1}H_{1.26}$	1.26	6.2469(7)	12.406(3)	1.008	30.25(1)	2.05	4.5	1.4
0.2	$Ti_{1.01}Ni_{0.79}Cu_{0.2}H_{1.30}$	1.30	6.254(1)	12.437(3)	1.006	30.40(1)	2.13	8.8	1.4
0.3	$Ti_{1.01}Ni_{0.69}Cu_{0.3}H_{1.25}$	1.25	6.254(8)	12.407(7)	1.008	30.32(3)	1.99	5.8	1.9
0.4	$Ti_{1.01}Ni_{0.59}Cu_{0.4}H_{1.11}$	1.11	6.257(2)	12.373(7)	1.011	30.28(2)	2.13	3.6	1.2
0.5	$Ti_{1.01}Ni_{0.49}Cu_{0.5}H_{1.08}$	1.08	6.264(4)	12.357(6)	1.014	30.30(4)	2.10	9.3	1.4

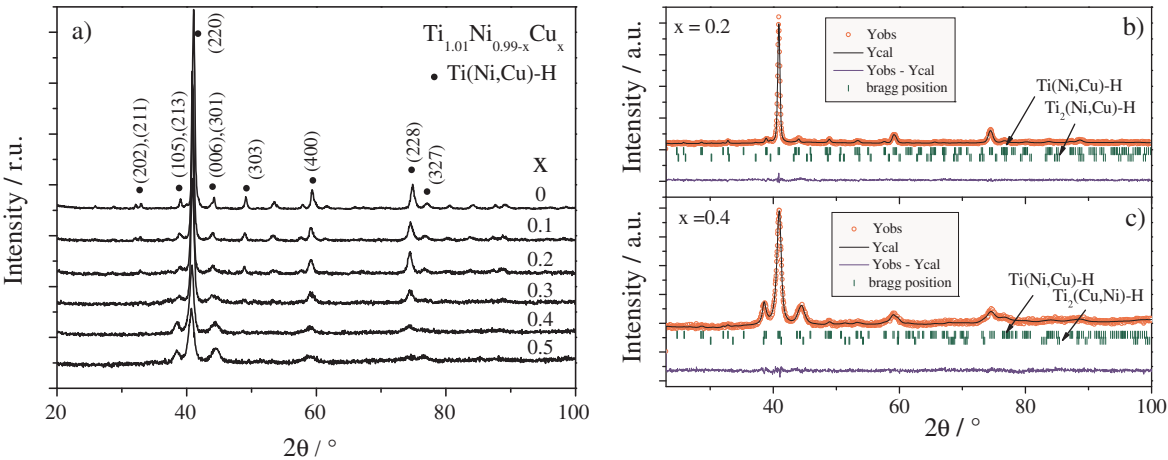


**Fig. 5.** a) XRD patterns for all hydrided  $Ti_{1.01}Ni_{0.99-x}Cu_x$  samples at RT. The main peaks for the tetragonal structure (S.G.  $I4/mmm$ ) are indexed. b) and c) Graphical outputs of the Rietveld analysis for  $Ti_{1.01}Ni_{0.79}Cu_{0.2}H_{1.3}$  and  $Ti_{1.01}Ni_{0.59}Cu_{0.4}H_{1.11}$  hydrided samples, respectively.

PXRD diffraction pattern for all fully hydrided samples are shown in Fig. 5a. Main diffraction peaks can be indexed in the tetragonal  $I4/mmm$  space group as previously reported for TiNi hydride with  $1 \leq C_H \leq 1.4$  [29]. The diffraction peaks broaden with increasing Cu content which indicates a progressive loss of crystallinity. Cell parameters and volume of the major Ti(Ni,Cu) hydride phase are gathered in Table 2. The  $a$  parameter gradually increases with Cu-content whereas the  $c$  parameter increases up to  $x = 0.2$  and then decreases. This results in a cell volume increase for Cu substitution up to  $x = 0.2$ , followed by a decrease at high Cu contents for which the tetragonal distortion ( $2a/c$  ratio) is reinforced. The cell volume increase is attributed to the enlargement of the

intermetallic sub-lattice with Cu substitution, whereas its decrease is due to the depletion in hydrogen content. It is worth noting that the volume occupied by the hydrogen atoms, determined as  $(V_{\text{hydride}} - V_{\text{IMC}})/C_H$ , is about  $2 \text{ \AA}^3 \text{ H}^{-1}$  in all compounds. This value concurs with previous findings in metals for which hydrogen atoms are localized in octahedral sites [29–31].

The diffraction patterns were analyzed by the Rietveld method. The results for two representative ( $x = 0.2$  and  $0.4$ ) samples are given in Table 3 and the graphical Rietveld output is shown in Fig. 5b and c. The crystal structure of the main  $Ti(Ni,Cu)H_y$  hydride phase can be refined assuming the random substitution of Cu atoms in Ni sites. The refined site occupancy factor (SOF) for Cu

**Table 3**  
The crystal structure of the metal sub-lattice of the main phase in  $Ti_{1.01}Ni_{0.79}Cu_{0.2}H_{1.3}$  and  $Ti_{1.02}Ni_{0.59}Cu_{0.4}H_{1.11}$  hydrides as obtained from the Rietveld analysis of PXRD data. The standard deviations referred to the last digit are given in parenthesis.

Site no.	Atoms	Wyckoff	$x$	$y$	$z$	SOF
$Ti_{1.01}Ni_{0.79}Cu_{0.2}H_{1.30}$ , S.G. $I4/mmm$ , $a = 6.254(1) \text{ \AA}$ , $c = 12.437(3) \text{ \AA}$ , $R_b (\%) = 8.8$ , $R_{wp} (\%) = 7.5$ , $\chi^2 = 1.4$						
1	Cu	16m	0.2789(5)	$x$	0.1321(6)	0.16(3)
	Ni					0.84(3)
2	Ti1	4e	0	0	0.233(1)	1
3	Ti2	4d	0	1/2	1/4	1
4	Ti3	4c	0	1/2	0	1
5	Ti4	2b	0	0	1/2	1
6	Ti5	2a	0	0	0	1
$Ti_{1.01}Ni_{0.59}Cu_{0.4}H_{1.11}$ , S.G. $I4/mmm$ , $a = 6.257(2) \text{ \AA}$ , $c = 12.373(7) \text{ \AA}$ , $R_b (\%) = 3.6$ , $R_{wp} (\%) = 3.3$ , $\chi^2 = 1.2$						
1	Cu	16m	0.2756(1)	$x$	0.1350(9)	0.44(5)
	Ni					0.56(5)
2	Ti1	4e	0	0	0.226(2)	1
3	Ti2	4d	0	1/2	1/4	1
4	Ti3	4c	0	1/2	0	1
5	Ti4	2b	0	0	1/2	1
6	Ti5	2a	0	0	0	1



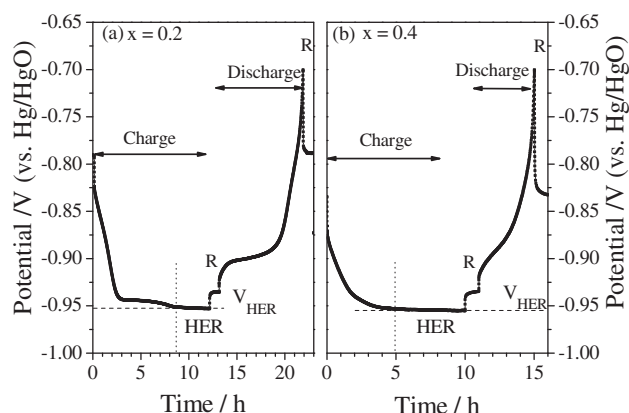


**Fig. 6.** Potential traces in the 4th cycle for  $\text{Ti}_{1.01}\text{Ni}_{0.99-x}\text{Cu}_x$  compounds with (a)  $x = 0.2$  and (b)  $x = 0.4$ . Horizontal and vertical dashed lines indicate the time and potential at which the hydrogen evolution reaction is detected.

atoms at 16m site is in good agreement with the nominal alloy composition:  $\text{SOF}_{\text{Cu},16\text{m}} = 0.16 \pm 0.03$  and  $0.43 \pm 0.05$  for  $x = 0.2$  and 0.4, respectively. Secondary hydride phases of the type  $\text{Ti}_2(\text{Ni,Cu})\text{-H}$  and  $\text{Ti}_2(\text{Cu,Ni})\text{-H}$  at low and high Cu-contents, respectively, were also detected at a typical content of 3 wt.%.

### 3.3. Electrochemical properties

#### 3.3.1. Galvanostatic cycling

Electrochemical properties of the  $\text{Ti}_{1.01}\text{Ni}_{0.99-x}\text{Cu}_x$  compounds were first investigated by galvanostatic cycling. Potential traces at the 4th cycle are shown in Fig. 6. For  $x = 0.2$ , the potential decreases rapidly on charging for 3 h due to solid solution of hydrogen in the  $\alpha$ -metal phase. Then, a wide plateau potential at  $-0.94$  V occurs for 6 h attributed to the  $\alpha$ -metal to  $\beta$ -hydride phase transformation. Next, the potential decreases to reach the potential of the hydrogen evolution reaction (HER) at  $-0.951$  V. On discharge, the reverse reactions are observed with a significant hysteresis in the potential plateau that occurs at  $-0.90$  V for the  $\beta \rightarrow \alpha$  phase transformation.

The potential trace for  $x = 0.4$  differs as compared to  $x = 0.2$ . For both charge and discharge no potential plateau is observed. On charging the potential gradually decreases for 4 h until the HER potential is attained. The reverse behavior is observed on discharge. On relaxation at the end of discharge, the potential decreases to lower value than for  $x = 0.2$ , which indicates that more hydrogen

keeps trapped within the electrode on increasing the Cu content. This suggests that the hydrogenation kinetics slows down with increasing Cu-content as observed in solid–gas experiments.

Electrochemical cycling was performed for all samples up to 30 cycles (Fig. 7a). All electrodes fully activate in three cycles. As proved for  $(\text{Ti,Zr})\text{Ni}$  compounds, this activation period probably corresponds to the modification of native oxides formed on the surface of active material [17]. Good cycling stability is observed for all electrodes with typical capacity decay lower than 0.2% per cycle except for  $\text{TiNi}_{0.8}\text{Cu}_{0.2}$ . The latter electrode, which exhibits the highest capacity, has a capacity loss of 0.6% by cycle. This is probably associated to pulverization effects related to the high amount of reversible hydrogen loading. Its maximum capacity attains  $300 \text{ mAh g}^{-1}$  which is very close to the discharge capacity of commercial-type  $\text{LaNi}_5$  compounds without containing expensive rare earth elements.

It is worth comparing the electrochemical capacities measured by galvanostatic cycling with those that can be calculated from the hydrogen content obtained by solid–gas reaction (Table 2). This is shown in Fig. 7b. The latter capacities constitute an upper limit of the former, since in open electrochemical cells the equivalent pressure is limited to 0.1 MPa. The electrochemical capacity first increases by Cu substitution from  $150$  to  $300 \text{ mAh g}^{-1}$  for  $x = 0$  and 0.2, respectively, and approaches the solid–gas limit of  $350 \text{ mAh g}^{-1}$ . Then, the electrochemical capacity gradually decreases down to  $96 \text{ mAh g}^{-1}$  for the highest Cu content ( $x = 0.5$ ). This behavior can be qualitatively understood after considering the destabilizing effect of Cu substitution, which is clearly revealed by the following GITT experiments.

#### 3.3.2. GITT isotherms

GITT isotherms at RT were obtained for electrodes with  $x \leq 0.2$  after activation. Results are shown in Fig. 8. Whereas no clear potential plateau is observed in binary  $\text{TiNi}$ , it happens with Cu substitution. This potential plateau shifts to lower potentials as the Cu substitution increases. Using the Nernst equation, equivalent plateau pressures of  $2 \times 10^{-3}$  and  $10^{-2}$  MPa are calculated for  $x = 0.1$  and 0.2 electrodes, respectively. This corroborates the destabilization of  $\text{Ti}(\text{Ni,Cu})$  hydride with Cu content as observed for PCI isotherms (Fig. 4). Moreover, Cu substitution opens a wide miscibility gap at room temperature between the  $\alpha$ -metal and  $\beta$ -hydride phases. Thus, the largest plateau is observed for  $x = 0.2$  Cu content which has the highest discharge capacity. For higher Cu contents, the potential plateau surpasses atmospheric pressure on charging (see Fig. 6b) and consequently the GITT isotherms (not

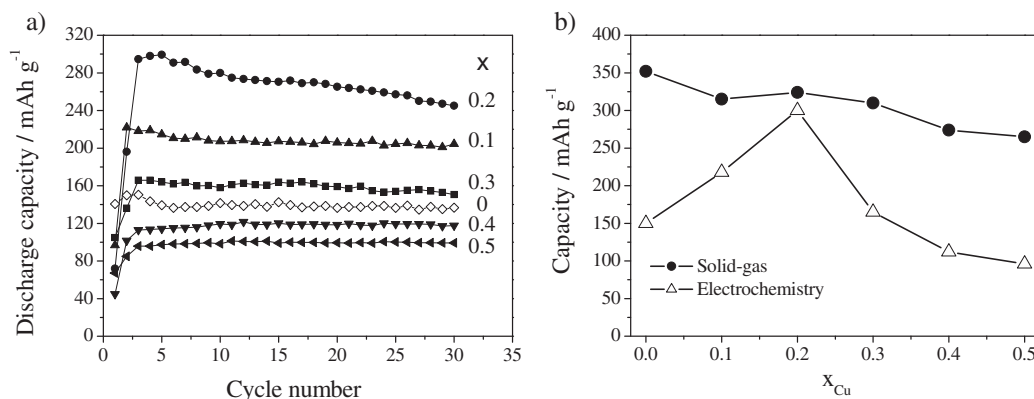


**Fig. 7.** a) Discharge capacity of  $\text{Ti}_{1.01}\text{Ni}_{0.99-x}\text{Cu}_x$  electrodes as a function of cycling number, b) comparison between the maximum electrochemical discharge capacity (open symbols) and the solid–gas capacity of  $\text{Ti}_{1.01}\text{Ni}_{0.99-x}\text{Cu}_x$  compounds in electrochemical units (full symbols).

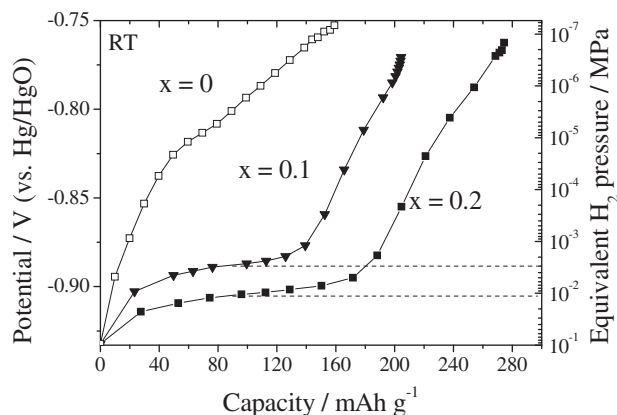


Fig. 8. Electrochemical GITT isotherms of  $\text{Ti}_{1.01}\text{Ni}_{0.99-x}\text{Cu}_x$  ( $x = 0, 0.1$  and  $0.2$ ) electrodes. Dashed lines show the equivalent plateau pressure at half plateau.

shown) do not exhibit any potential plateau. This also accounts for the observed decrease on the discharge capacity for  $x \geq 0.3$  (Fig. 7b).

### 3.3.3. High-rate capability

The interesting electrochemical properties of  $\text{Ti}_{1.01}\text{Ni}_{0.79}\text{Cu}_{0.2}$  compound deserve further electrochemical characterization. High-rate capability measurements were performed on this compound and compared to binary  $\text{Ti}_{1.01}\text{Ni}_{0.99}$ . Kinetic results are shown in Fig. 9. Since these measurements were conducted on discharge, rate capabilities are denoted hereafter as D instead of the more usual C notation. Both electrodes start providing significant discharge capacities at D rate. However, the Cu substituted compound exhibit better kinetics than the binary one. At D/2 rate, 80% of its maximum capacity is obtained for the former whereas only 40% is obtained for the latter. This result shows that  $\text{Ti}_{1.01}\text{Ni}_{0.79}\text{Cu}_{0.2}$  compound can be used at significant rates with 80% discharge in 2 h. Such a good kinetics obtained at room temperature is striking when compared with the slow kinetics observed by solid–gas reaction at 423 K. This may indicate that the surface reactivity is higher in electrochemical than in solid/gas medium.

## 3.4. In-situ neutron diffraction studies

We have shown that Cu substitution enhances the reversible electrochemical capacity of TiNi from  $150 \text{ mAh g}^{-1}$  to  $300 \text{ mAh g}^{-1}$  due to the enlargement of the  $\alpha$ – $\beta$  miscibility gap and also to the decrease of the hydride stability. To better understand this behavior, the structural transformations of  $\text{Ti}_{1.01}\text{Ni}_{0.99}$  and  $\text{Ti}_{1.01}\text{Ni}_{0.79}\text{Cu}_{0.2}$  compounds were investigated during their electrochemical deuteration by in-situ neutron powder diffraction.

### 3.4.1. $\text{Ti}_{1.01}\text{Ni}_{0.99}$ electrode

Structural transformations for the  $\text{Ti}_{1.01}\text{Ni}_{0.99}$  electrode were investigated during the first electrochemical cycle. The electrode was charged with a constant current of  $-34 \text{ mA g}^{-1}$  (i.e. C/10 rate) for 12 h, relaxed for 1.5 h in open circuit, and discharged at D/10 rate up to the potential of 0.5 V versus Cd/Cd(OD)<sub>2</sub>. The time evolution of NPD pattern in the angular domain  $23 < 2\theta < 35$  during the first cycle is shown in Fig. 10. Unfortunately, the main diffraction peaks of the IMC phase as well as those of electrochemically formed hydrides are superposed into a broad diffraction bump originated by diffuse scattering of the electrolyte and silica container. This fact renders difficult here and in forthcoming analysis to extract detailed crystallographic information. Nevertheless, on charging,

one can note the gradual vanishing of the diffraction peaks referring to the  $\alpha$ -B19' IMC phase and the appearance of a new set of diffraction peaks corresponding to the formation of  $\beta$ -deuteride. Moreover, the diffraction peaks of the  $\beta$ -phase shift to lower angles suggesting an extended solid solution range of deuterium in this phase. The peaks of the deuteride phase can be indexed in the S.G.  $I4/mmm$  as occurs for solid–gas experiments (Fig. 5).

The maximum deuterium loading attained by electrochemical means has been determined by Rietveld analysis of the NPD pattern monitored at the end of charge. The Rietveld graphical output is shown in Fig S2 of Supplementary material. The deuterium content reaches  $1.3 \pm 0.1 \text{ D f.u.}^{-1}$ . This value concurs with the hydrogen capacity of TiNi compound through solid–gas reaction at normal conditions of pressure and temperature [13]. This state is denoted as  $\beta_{\text{max}}$ -phase in Fig. 10. On discharge, the deuterium content of the  $\beta$ -phase decreases down to  $1.0 \pm 0.1 \text{ D f.u.}^{-1}$ . This state is denoted as  $\beta_{\text{min}}$ -phase. In addition a new peak located at  $2\theta = 29.2^\circ$  appears at the end of the discharge. Its position differs from those of  $\alpha$  and  $\beta$  phases. It is attributed to the formation of a new phase denoted as  $\gamma$ -phase. Diffraction peaks from this phase could be tentatively indexed in the S.G.  $P4/mmm$ , but its deuterium content could not be determined by Rietveld analysis. However, it can be estimated from the expansion of the metal sub-lattice cell volume considering, as shown before, that hydrogen occupies  $\sim 2 \text{ \AA}^3 \text{ H}^{-1}$  in TiNi-based compounds. Thus, the hydrogen content in the  $\gamma$  phase is estimated as  $C_{\text{HV}} = 0.63 \text{ D f.u.}^{-1}$ .

For the whole galvanostatic cycle, cell parameters and amount of detected phases have been sequentially refined by Rietveld analysis. Fig. 11 shows these results together with the electrochemical charge Q passed through the electrode. During the charging step, no solid solution domain of deuterium in the  $\alpha$ -phase is observed and the volume of this phase keeps almost constant. Indeed, a two phase domain exists where the  $\alpha$ -phase transforms into the  $\beta$ -deuteride phase. The volume of the  $\beta$ -phase increases continuously which confirms high solubility of deuterium in this phase. Deuterium gas evolution occurs beyond 10 h as a result of  $\beta$ -deuteride saturation at 1 atm. On discharge, the amount of  $\beta$ -phase is initially constant ( $13.5 < t < 15.5 \text{ h}$ ) but the cell volume of the  $\beta$ -phase decreases as a result of deuterium unloading from the  $\beta$ -phase. Within this region  $70 \text{ mAh g}^{-1}$  of discharge capacity are obtained. Later, from 15.5 h to 17.3 h, a two phase domain is observed where the  $\beta$ -phase partially transforms into the  $\gamma$  phase. The maximum amount of  $\gamma$  phase at the end of charge is 10 wt.%. The total discharge capacity reaches  $130 \text{ mAh g}^{-1}$  which is equivalent to the discharge of  $0.52 \text{ D f.u.}^{-1}$ .

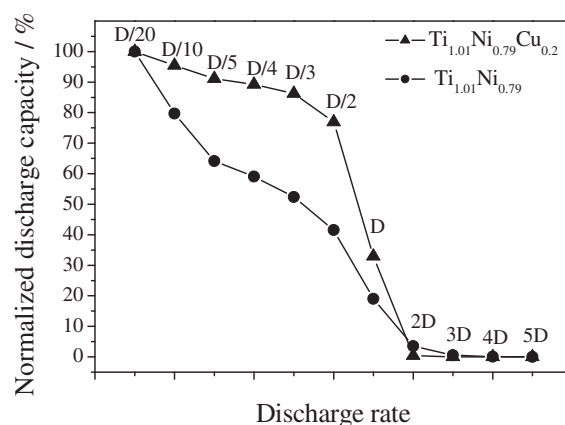


Fig. 9. Evolution of normalized discharge capacity versus the discharge rate for  $\text{Ti}_{1.01}\text{Ni}_{0.99}$  and Cu substituted  $\text{Ti}_{1.01}\text{Ni}_{0.79}\text{Cu}_{0.2}$ .

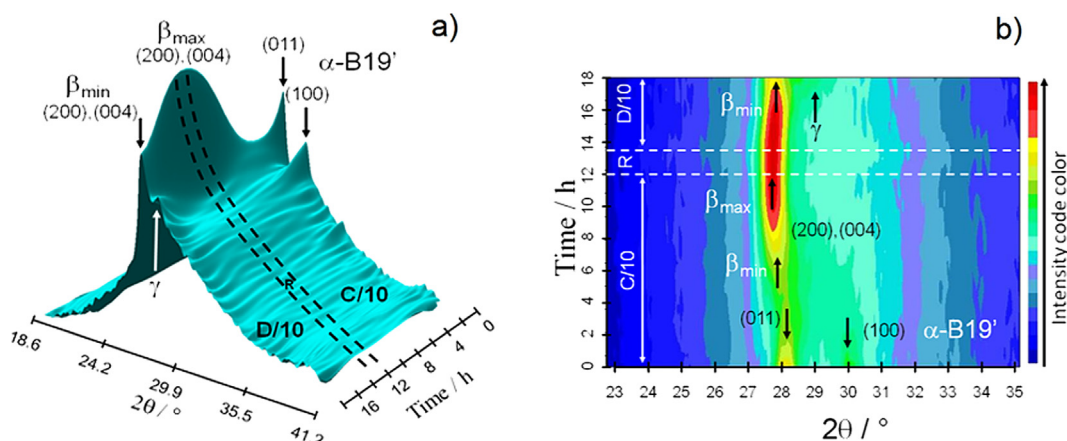


Fig. 10. 3D (left) and 2D (right) view of the NPD pattern evolution as function of time during the first charge and discharge cycle of TiNi electrode.

As a final remark for this electrode, it is worth nothing that the crystal structure of the  $\beta$ -deuteride phase (S.G.  $I4/mmm$ ) is the same by electrochemical charging at RT and by solid–gas reaction at 473 K. However, the crystal structure of the pristine  $\text{Ti}_{1.01}\text{Ni}_{0.99}$  compound differs in these experiments: B19' at RT and B2 at 473 K. It is therefore concluded that neither TiNi polymorphism nor hydrogenation route (electrochemical vs. solid–gas reaction) influence the crystal structure of the formed hydride phase.

To summarize, electrochemical charging of  $\text{Ti}_{1.01}\text{Ni}_{0.99}$  electrode induces  $\alpha$ -metal to  $\beta$ -hydride phase transformation with the end formation of  $\text{TiNiD}_{1.3\pm0.1}$  compound. This corresponds to a charge capacity of  $330 \text{ mAh g}^{-1}$ . On discharge, only  $130 \text{ mAh g}^{-1}$  (i.e.  $0.52 \text{ D f.u.}^{-1}$ ) are recovered, mostly as result of deuterium depletion within the  $\beta$ -hydride phase.

### 3.4.2. $\text{Ti}_{1.01}\text{Ni}_{0.79}\text{Cu}_{0.2}$ electrode

*In-situ* NPD studies were next performed on  $\text{Ti}_{1.01}\text{Ni}_{0.79}\text{Cu}_{0.2}$  electrode during the first galvanostatic cycling. 3D NPD patterns during cycling at C/10–D/10 regime are shown in Fig. 12a. The pristine active material crystallizes in the B19 structure (S.G.  $Pmmb$ ) denoted here as  $\alpha$ -B19 phase. On charging, diffraction peaks from this phase disappear but no novel peaks are observed. It can be inferred that deuterium loading leads in this case to the formation of a poorly-crystallized phase. On discharging, diffraction peaks show up again but at positions that differ from those of the pristine  $\alpha$ -B19 phase. These peaks could alternatively be indexed in the monoclinic  $P2_1/m$  space group, astonishingly the same as for pristine binary compound. Indeed, the lattice parameters and cell

volume of this phase are close (though slightly larger) to the binary TiNi electrode (see Table 4). Its deuterium content was evaluated from the cell volume expansion as  $0.28 \text{ H f.u.}^{-1}$ . This low value indicates that, on discharge, an intermetallic phase having small deuterium solubility is formed. This phase is denoted as  $\alpha'$  since its structure differs from that of the pristine  $\alpha$ -B19 phase.

For the first galvanostatic cycle, the electrode only discharged  $235 \text{ mAh g}^{-1}$ . We previously showed that at least three cycles are needed for this compound to achieve full activation (Fig. 7). Then, the electrode was further cycled out of beam for three times and charged again. Contrary to the first charging, the NPD after at the fourth charge exhibited diffraction peaks that could be tentatively indexed in the S.G.  $I4/mmm$  as for  $\text{Ti}(\text{Ni,Cu})$   $\beta$ -deuterides prepared by solid–gas reaction (Fig. 5). However, this deuterated phase exhibits markedly distinct lattice parameters and will be thereafter denoted as  $\beta'$ -phase. In particular, using this indexing, the cell volume of this phase is strikingly large ( $31.38 \text{ \AA}^3 \text{ f.u.}^{-1}$ ), leading to an estimated D-content of  $1.84 \text{ D f.u.}^{-1}$ . This value is probably over-estimated as will be later shown and may indicate that the structural assignment is not fully correct. Unfortunately, the quality of the diffraction patterns did not allow a more accurate analysis.

The  $\text{Ti}_{1.01}\text{Ni}_{0.79}\text{Cu}_{0.2}$  electrode was charged again in beam at a C/5 ( $-71.32 \text{ mA g}^{-1}$ ) rate to ensure full deuteration. The electrode was then discharged sequentially at D/5, D/10 and D/20 rate with relaxation periods between each discharge step. The corresponding 3D view of NPD patterns is shown in Fig. 12b. No significant change is observed on charging at C/5. On discharge, the diffraction lines belonging to deuterium rich  $\beta'$ -phase decrease in intensity whereas

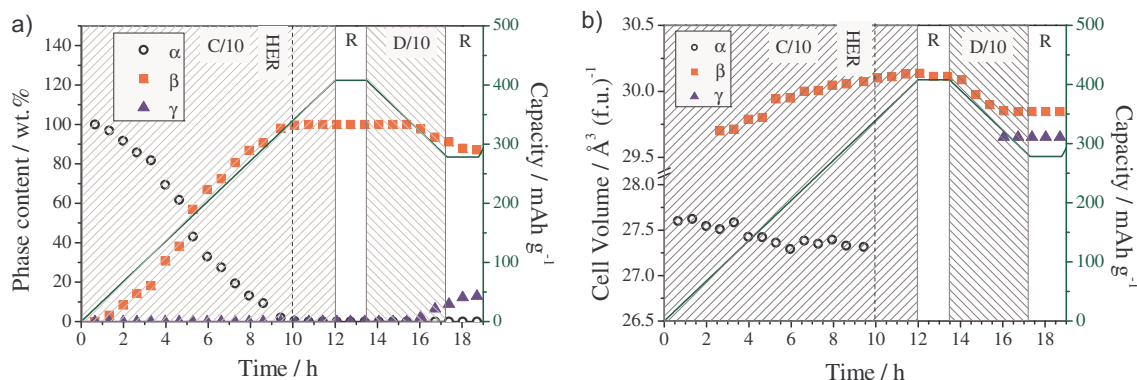
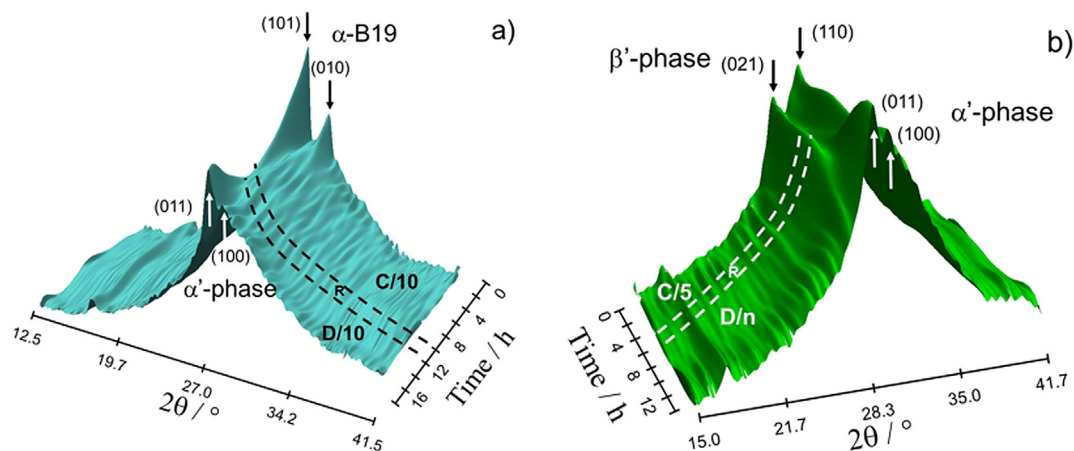


Fig. 11. Evolution of (a) phase amount and (b) cell volume for the  $\alpha$ ,  $\beta$  and  $\gamma$  phases during the *in situ* charge at C/10 and discharge at D/10 of TiNi electrode.





**Fig. 12.** 3D in-situ NPD patterns of  $\text{Ti}_{1.01}\text{Ni}_{0.79}\text{Cu}_{0.2}$  electrode. a) first charge/discharge cycle, b) charging (C/5) and discharging steps (D/n with  $n = 5, 10$  and  $20$  successively) in the fourth galvanostatic cycle. Phase identification and indexation of main peaks are given.

**Table 4**

Cell parameters, volume and deuterium content of detected phases in  $\text{Ti}_{1.01}\text{Ni}_{0.99}$  and  $\text{Ti}_{1.01}\text{Ni}_{0.79}\text{Cu}_{0.2}$  electrodes during in-situ NPD electrochemical experiments.  $C_{\text{HR}}$  and  $C_{\text{HV}}$  state for the deuterium content in detected phases as determined by Rietveld refinement and cell-volume changes, respectively.

Electrode	Phase	S.G.	$a$ ( $\text{\AA}^3$ )	$b$ ( $\text{\AA}^3$ )	$c$ ( $\text{\AA}^3$ )	$\beta$ ( $^\circ$ )	$V$ ( $\text{\AA}^3 \text{ f.u.}^{-1}$ )	$C_{\text{HR}}$ (D f.u. $^{-1}$ )	$C_{\text{HV}}$ (D f.u. $^{-1}$ )
TiNi	$\alpha$ -B19'	$P2_1/m$	2.911(1)	4.116(1)	4.652(2)	97.67(3)	27.67(1)		0
	$\beta_{\text{max}}$	$I4/mmm$	6.231(1)	6.231(1)	12.418(5)		30.14(2)	1.3(1)	1.24
	$\beta_{\text{min}}$	$I4/mmm$	6.216(2)	6.216(2)	12.409(7)		29.84(2)	1.0(1)	1.09
	$\gamma$	$P4/mmm$	3.123(2)	3.123(2)	2.966(3)		28.93(3)		0.63
$\text{TiNi}_{0.8}\text{Cu}_{0.2}$	$\alpha$ -B19	$Pmmb$	2.894(2)	4.236(2)	4.519(2)		27.71(2)		0
	$\alpha'$	$P2_1/m$	2.977(3)	4.113(3)	4.65 <sup>a</sup>	97 <sup>a</sup>	28.26(4)		0.28
	$\beta'$	$I4/mmm$	6.464(3)	6.464(3)	12.018(9)		31.38(4)		1.84

<sup>a</sup> Not refined.

those of the previously described  $\alpha'$ -phase increase. The total discharge capacity reaches  $330 \text{ mAh g}^{-1}$  at D/20 which corresponds to a reversible deuterium loading of  $1.32 \text{ D f.u.}^{-1}$ . From this result and the deuterium content of the  $\alpha'$ -phase ( $0.28 \text{ D f.u.}^{-1}$ ), one may re-evaluate more correctly the deuterium content of the  $\beta'$  phase as  $1.6 \text{ D f.u.}^{-1}$ .

Rietveld analysis has been sequentially performed for the discharge step. Phase contents are displayed in Fig. 13. On discharging, a gradual two-phase transformation from the D-rich  $\beta'$ -phase to the D-poor  $\alpha'$ -phase is observed. At the end of discharge, the transformation is almost complete reaching 93% of  $\alpha'$ -phase.

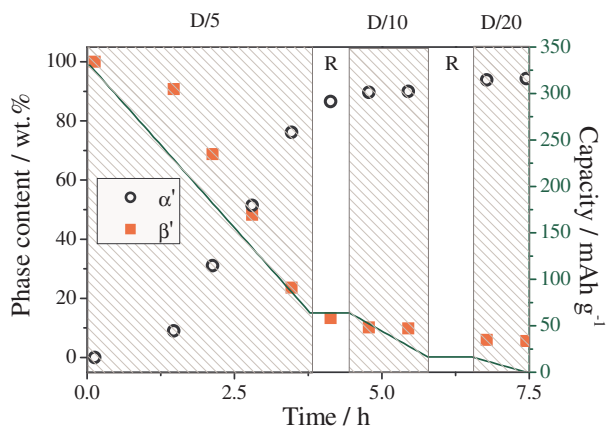


**Fig. 13.** Evolution of phase amounts during the *in situ* electrochemical discharge of  $\text{Ti}_{1.01}\text{Ni}_{0.79}\text{Cu}_{0.2}$  electrode during the fourth galvanostatic cycle.

To summarize,  $\text{Ti}_{1.01}\text{Ni}_{0.79}\text{Cu}_{0.2}$  electrode discharges reversibly up to  $330 \text{ mAh g}^{-1}$  at D/20 rate after complete activation. Contrary to  $\text{Ti}_{1.01}\text{Ni}_{0.99}$ , where discharge capacity originates from depleting of deuterium within the  $\beta$ -deuteride solid solution, the high discharge capacity of  $\text{TiNi}_{0.8}\text{Cu}_{0.2}$  electrode results from a two phase transformation between D-rich and D-poor phases with approximate deuterium contents of  $1.6$  and  $0.3 \text{ D f.u.}^{-1}$ , respectively. The crystal structure of these electrochemically formed phases could not be fully resolved but seem to differ from those obtained by solid–gas reaction. The determination of their crystallographic properties requires further investigation.

#### 4. Conclusion

Binary TiNi forms under normal conditions of hydrogen pressure and temperature a  $\text{TiNiH}_{1.4}$  hydride. If the stored hydrogen content could be fully discharged, the electrochemical capacity of this compound would reach  $352 \text{ mAh g}^{-1}$ , a value in the range of current commercial electrodes. Unfortunately, the observed experimental discharge capacity of this compound is only  $150 \text{ mAh g}^{-1}$ . Such a low capacity is due to the fact that, only hydrogen stored as solid solution in the hydride phase can be recovered by electrochemical means.

Ni for Cu substitution in TiNi leads to the formation of pseudo-binary  $\text{Ti}(\text{Ni,Cu})$  compounds. Cu substitution destabilizes the hydride phase and opens a wide miscibility gap in the electrochemical isotherms. Thus, for 20% of Cu substitution, the electrochemical plateau potential is slightly below atmospheric pressure leading to an optimum in discharge capacity. The capacity of  $\text{TiNi}_{0.8}\text{Cu}_{0.2}$  compound attains  $300 \text{ mAh g}^{-1}$  at D/10 regime as result of a reversible metal to hydride phase transformation. This compound

exhibits interesting cycle life and good kinetics below D/2 regime. Interestingly, these properties approach those of current commercial electrodes without using expensive rare earth metals, making TiNi-based electrodes a promising system for next generation of NiMH batteries.

## Acknowledgments

The authors wish to acknowledge E. Leroy for EMPA analysis and D. Sheptyakov for his help in ND experiments at PSI (Switzerland).

## Appendix A. Supplementary data

Supplementary data related to this article can be found at <http://dx.doi.org/10.1016/j.jpowsour.2014.04.114>.

## References

- [1] U. Eberle, M. Felderhoff, F. Schuth, *Angew. Chem. Int. Ed.* 48 (2009) 6608–6630.
- [2] M. Latroche, *J. Phys. Chem. Sol.* 65 (2004) 517–522.
- [3] F. Cuevas, J.-M. Joubert, M. Latroche, A. Percheron-Guégan, *Appl. Phys. A* 72 (2001) 225–238.
- [4] Y. Liu, H. Pan, M. Gao, Q. Wang, *J. Mater. Chem.* 21 (2011) 4743–4755.
- [5] K.H. Young, J. Nei, *Materials* 6 (2013) 4574–4608.
- [6] P.H.L. Notten, M. Latroche, in: J. Garche (Ed.), *Encyclopedia of Electrochemical Power Sources*, Elsevier, Amsterdam, 2009, pp. 502–521.
- [7] K. Kadir, I. Uehara, T. Sakai, *J. Alloys Compd.* 257 (1997) 115–121.
- [8] T. Kohno, H. Yoshida, M. Kanda, *J. Alloys Compd.* 363 (2004) 249–252.
- [9] T. Ozaki, M. Kanemoto, T. Takeya, Y. Kitano, M. Kuzuhara, M. Watada, S. Tanase, T. Sakai, *J. Alloys Compd.* 446–447 (2007) 620–624.
- [10] J. Van Humbeeck, *Adv. Eng. Mater.* 3 (2001) 837–850.
- [11] S. Shabalovskaya, *Biomed. Mater. Eng.* 12 (2002) 69–109.
- [12] K. Otsuka, X. Ren, *Prog. Mater. Sci.* 50 (2005) 511–678.
- [13] R. Burch, N.B. Mason, *J. Chem. Soc. Faraday Trans. I* 75 (1979) 561–577.
- [14] E.W. Justi, H.H. Ewe, A.W. Kalberlah, N.M. Saridakis, M.H. Schaefer, *Energy Convers.* 10 (1970) 183–187.
- [15] M.A. Gutjahr, H. Buchner, K.D. Beccu, H. Säufler, *Power Sources* 4 (1973) 79–91.
- [16] B. Guiose, F. Cuevas, B. Décamps, A. Percheron-Guégan, *Int. J. Hydrogen Energy* 33 (2008) 5795–5800.
- [17] B. Guiose, F. Cuevas, B. Décamps, E. Leroy, A. Percheron-Guégan, *Electrochim. Acta* 54 (2009) 2781–2789.
- [18] M. Latroche, Y. Chabre, B. Decamps, A. Percheron-Guégan, D. Noréus, *J. Alloys Compd.* 334 (2002) 267–276.
- [19] J. Rodríguez-Carvajal, *Phys. B* 192 (1993) 55–69.
- [20] K.P. Gupta, *J. Phase Equilib.* 23 (2002) 541–547.
- [21] T.H. Nam, T. Saburi, K. Shimizu, *Mater. Trans. JIM* 31 (1990) 959–967.
- [22] J.-L. Murray, in: J.-L. Murray (Ed.), *ASM International, Metals Park, Ohio, 1987*, p. 159.
- [23] J.-C. Achard, A. Percheron-Guégan, H. Diaz, F. Briaucourt, F. Demany, in: *2nd Int. Congress on Hydrogen in Metals, 1977*, p. 1E12.
- [24] C.E. Lundin, F.E. Lynch, C.B. Magee, *J. Less-Common Met.* 56 (1977) 19–37.
- [25] H. Emami, F. Cuevas, *Intermetallics* 19 (2011) 876–886.
- [26] H. Emami, R. Souques, J.C. Crivello, F. Cuevas, *J. Solid State Chem.* 198 (2013) 475–484.
- [27] R. Kadel, A. Weiss, *Ber. Bunsenges. Phys. Chem.* 82 (1978) 1290–1302.
- [28] G. Mazzolai, *J. Alloys Compd.* 446–447 (2007) 204–207.
- [29] J.-L. Soubeyroux, D. Fruchart, G. Lorthioir, P. Ochir, D. Colin, *J. Alloys Compd.* 196 (1993) 127–132.
- [30] F. Cuevas, M. Latroche, F. Bouree-Vigneron, A. Percheron-Guegan, *J. Solid State Chem.* 179 (2006) 3295–3307.
- [31] Y. Fukai, *The Metal–Hydrogen System*, vol. 21, Springer-Verlag, 1992.